

## REPORT DOCUMENTATION PAGE

AFRL-SR-AR-TR-03-

Public reporting burden for this collection of information is estimated to average 1 hour per response, including the time for reviewing instruction the collection of information. Send comments regarding this burden estimate or any other aspect of this collection of information, including Operations and Reports, 1215 Jefferson Davis Highway, Suite 1204, Arlington, VA 22202-4302, and to the Office of Management and Budget,

and reviewing  
or Information

0090

1. AGENCY USE ONLY (Leave blank)		2. REPORT DATE	3. REPORT TYPE AND DATES COVERED 15 Mar 00 to 28 Feb 03 FINAL	
4. TITLE AND SUBTITLE Computer Simulations of Microwave Generation from Relativistic Electron Beams			5. FUNDING NUMBERS 61102F 2301/EX	
6. AUTHOR(S) Dr Lin				
7. PERFORMING ORGANIZATION NAME(S) AND ADDRESS(ES) UNIVERSITY OF CALIFORNIA 1401 UEBERROTH BLDG BOX 951406 LOS ANGELES CA 90095-1406			8. PERFORMING ORGANIZATION REPORT NUMBER	
9. SPONSORING/MONITORING AGENCY NAME(S) AND ADDRESS(ES) AFOSR/NE 4015 WILSON BLVD SUITE 713 ARLINGTON VA 22203			10. SPONSORING/MONITORING AGENCY REPORT NUMBER  F49620-00-1-0185	
11. SUPPLEMENTARY NOTES				
12a. DISTRIBUTION AVAILABILITY STATEMENT APPROVED FOR PUBLIC RELEASE, DISTRIBUTION UNLIMITED			12b. DISTRIBUTION CODE	
13. ABSTRACT (Maximum 200 words) This is the Final Technical Report on work performed under the support of the Air Force Office of Scientific Research on the subject of simulating microwave generation. This report contains the write-ups that we sent for the upcoming book on power vacuum electronics. The first section (Chapter 10) describes the simulation algorithm based on mode expansion technique developed at UCLA while the second section (Chapter 5) gives the real amplification mechanism for the Phigtron.				
14. SUBJECT TERMS			15. NUMBER OF PAGES	
			16. PRICE CODE	
17. SECURITY CLASSIFICATION OF REPORT  UNCLASSIFIED		18. SECURITY CLASSIFICATION OF THIS PAGE  UNCLASSIFIED	19. SECURITY CLASSIFICATION OF ABSTRACT  UNCLASSIFIED	20. LIMITATION OF ABSTRACT  UL

20030508 149

# **Computer Simulations of Microwave Generation From Relativistic Electron Beams**

F49620-00-1-0185

FINAL TECHNICAL REPORT

TO

AIR FORCE OFFICE OF SCIENTIFIC RESEARCH

Dr. Anthony T. Lin

Department of Physics

University of California, Los Angeles

Los Angeles, CA 90024-1547

Dec. 1, 2002 to Mar. 15, 2003

## **Computer Simulations of Microwave Generation From Relativistic Electron Beams**

This is the Final Technical Report on work performed under the support of the Air Force Office of Scientific Research on the subject of simulating microwave generation. This report contains the write-ups that we sent for the upcoming book on power vacuum electronics. The first section (Chapter 10) describes the simulation algorithm based on mode expansion technique developed at UCLA while the second section (Chapter 5) gives the real amplification mechanism for the Phigtron.

### **I. Mode Expansion Technique (METPIC)**

#### **A. Introduction**

Using the Coulomb gauge, an algorithm for solving Maxwell's equations that is capable of isolating the solenoidal current component from the total current has been developed. The electromagnetic field arising from the solenoidal current is expanded in terms of Bessel-Fourier's functions. It is sufficient to retain only a few dominant global electromagnetic modes to simulate most microwave devices. Electrostatic modes that are localized within the beam region are followed by utilizing B-splines. This mode expansion technique is most effective in addressing basic physical issues involved in microwave devices with simple boundary conditions.

The electron-wave interaction in microwave devices is a highly nonlinear phenomenon and requires computer simulations to follow its evolution. The electron convection current calculated in simulation often contains both the electromagnetic and electrostatic components. This total current is usually used as the source for exciting the electric and magnetic fields in electrodynamic structures. With this approach, it is important to make sure that the equation of continuity is satisfied at all times. In MAGIC<sup>1</sup>, this is accomplished by correcting the electric field at every time step to ensure that Poisson's equation is satisfied. Most of the other approaches employed to simulate microwave devices are for medium electron beam current and assume fixed transverse field profiles determined from the boundary conditions of the structure. The electrostatic field evaluated from the Poisson equation is often added to the fields generated by the total current. In doing so, the dominant mode of space charge fields may be doubly counted. In order to be able to correctly investigate the effects of space charge field on the performance of microwaves devices, a new algorithm for solving Maxwell's equations which is capable of isolating the solenoidal current from the total current have been developed.

Since early seventies, particle simulations based on the Fast Fourier Transform (FFT) technique to solve Maxwell's equations have been in use in plasma physics and radiation generation<sup>2,3</sup> at Princeton Plasma Lab and UCLA. In 1982, Caplan applied the

mode expansion technique to simulate Gyrotron Devices<sup>4</sup>. In microwave devices, a cylindrical waveguide is often provided to confine the electromagnetic wave propagation along the axial direction. A combination of Bessel's functions can always be found to satisfy the proper radial boundary conditions and Maxwell's equations. The field quantity can be expanded into a series of Bessel's functions that are complete orthogonal functions. For electromagnetic wave problems, the field in the exterior of the electron beam takes the form of a wave moving outwards if there is no structure to confine the wave propagation. In a cylindrical waveguide, the transverse mode becomes a global mode and retaining a few modes is often sufficient to evaluate the performance of microwave devices. Along the axial direction, the Fourier series expansion can be used to represent the self-consistent field profile that plays an important role in determining the efficiency of microwave devices.

## B. Solenoidal Current Component

By using the Coulomb gauge<sup>5</sup>, the current density (or electric field) can be decomposed into two terms,

$$\vec{J} = \vec{J}_l + \vec{J}_t \quad (1)$$

$J_l$  is the longitudinal (irrotational,  $\nabla \times \vec{J}_l = 0$ ) current component and is the driving source for electrostatic fields, while  $\vec{J}_t$  is the transverse (solenoidal,  $\nabla \cdot \vec{J}_t = 0$ ) current component and is the driving source for electromagnetic fields. The magnetic field, of course, only has transverse component. Starting from the vector identity,

$$\nabla \times (\nabla \times \vec{J}) = \nabla (\nabla \cdot \vec{J}) - \nabla^2 \vec{J} \quad (2)$$

the transverse current can be determined from the total current

$$\nabla^2 (\vec{J}_t) = -\nabla \times \nabla \times \vec{J} = \nabla^2 \vec{J} - \nabla (\nabla \cdot \vec{J}) \quad (3)$$

The solution of Eq. (3) in integral form is<sup>5</sup>

$$\vec{J}_t = \frac{1}{4\pi} \nabla \times \nabla \times \int \frac{\vec{J}}{(\vec{x} - \vec{x}')} d^3x' \quad (4)$$

This form of solution is difficult to obtain numerically. In the differential formulation, Eq. (3) can be easily solved if the field quantity is expanded into a series of complete orthogonal functions. For example, sets of such functions are the Fourier series and the Bessel functions which are the solutions for cylindrical waveguides.

Consider an infinite and periodic system. In this case, it is convenient to solve Maxwell's equations in the Fourier space<sup>3</sup> and the splitting of the current into transverse and longitudinal components can be easily done. From Eq. (3), the transverse current can

be written as

$$\vec{J}_t = \vec{J} - \frac{\vec{k}(\vec{k} \cdot \vec{J})}{k^2} \quad (5)$$

where  $\vec{k}$  is the wave vector. Based on this approach, for the last three decades, numerous interesting nonlinear phenomena in plasma physics<sup>3</sup> have been unraveled.

In microwave devices, a cylindrical waveguide (r,θ,z) is often employed to guide the electromagnetic wave axial propagation. The electromagnetic fields in a cylindrical waveguide with a constant cross-section can be expanded in terms of TE and TM modes as follows. For TE modes<sup>4</sup>

$$\vec{E}_{mn} = \sum_{p=1,2} E_{Tmn}^p(z,t) (\hat{z} \times \nabla_{\perp} C_{mn}^p) \quad (6)$$

$$\vec{B}_{mn} = - \sum_{p=1,2} [B_{Tmn}^p(z,t) \nabla_{\perp} C_{mn}^p + \hat{z} B_{Lmn}^p k_{mn} C_{mn}^p],$$

where the circular wave functions for the two polarizations are given by

$$C_{mn}^{1,2} = -\frac{2r_w}{k_{mn}} J_m \left[ \frac{k_{mn} r}{r_w} \right] [\cos m\theta, \sin m\theta] \quad (7)$$

and  $J'_m(k_{mn}) = 0$ . Here,  $r_w$  is the waveguide radius. For TM modes

$$\vec{E}_{mn} = - \sum_{p=1,2} [E_{Tmn}^p(z,t) \nabla_{\perp} C_{mn}^p + \hat{z} E_{Lmn}^p k_{mn} C_{mn}^p], \quad (8)$$

$$\vec{B}_{mn} = \sum_{p=1,2} B_{Tmn}^p(z,t) (\hat{z} \times \nabla_{\perp} C_{mn}^p),$$

where  $J_m(k_{mn}) = 0$ .

Take the spatial variation of the electron beam current to conform the electric field variation. For TE modes, substituting Eq. (6) into Eq. (3) yields  $\nabla(\nabla \cdot \vec{J}) = 0$  and thus  $\vec{J}_t = \vec{J}$  (excluding the spatially uniform current). For TM modes, as a simple example, an algorithm under the assumption of axial symmetry is developed. In this situation, the electric fields are along the z and r directions and only these current components ( $J_z$  and  $J_r$ ) needs to be retained as the source for exciting the electromagnetic field

$$\vec{J} = [\hat{z} J_z J_0(k_{0n} \frac{r}{r_w}) + \hat{r} J_r J_1(k_{0n} \frac{r}{r_w})] e^{ik_z z} \quad (9)$$

where  $k_{0n}$  is the zero of the Bessel function  $J_0$ .

The second term of the right-hand side of Eq. (3) becomes

$$\begin{aligned} \nabla (\nabla \cdot \vec{J}) = & \left[ \hat{z} \left( -k_z^2 J_z + \frac{ik_z k_{0n}}{r_w} J_r \right) J_0 \left( \frac{k_{0n} r}{r_w} \right) \right. \\ & \left. + \hat{r} \left( -ik_z \frac{k_{0n}}{r_w} J_z - \frac{k_{0n}^2}{r_w^2} J_z \right) J_1 \left( \frac{k_{0n} r}{r_w} \right) \right] e^{ik_z z}. \end{aligned} \quad (10)$$

The solenoidal current (Eq. 3) can thus be written as

$$\begin{aligned} J_{tz} = & - \left( \frac{k_{0n}^2}{r_w^2} J_z + \frac{ik_z k_{0n}}{r_w} J_r \right) J_0 \left( \frac{k_{0n} r}{r_w} \right) e^{ik_z z} / \left( \frac{k_{0n}^2}{r_w^2} + k_z^2 \right), \\ J_{tr} = & - \left( k_z^2 J_r - \frac{ik_z k_{0n}}{r_w} J_z \right) J_1 \left( \frac{k_{0n} r}{r_w} \right) e^{ik_z z} / \left( \frac{k_{0n}^2}{r_w^2} + k_z^2 \right). \end{aligned} \quad (11)$$

Notice that Eq.(11) is divergence free. These currents are retained as the source to advance the electromagnetic fields through Maxwell's equations.

### C. Nonuniform Waveguide Wall

The nonuniformity in waveguide wall causes the modes of the waveguide to couple among each other. There are at least two different ways to describe this mode coupling process. In the configuration that uses a taper to connect two uniform waveguide such as the extended interaction cavity, the most convenient way is to expand the electromagnetic field of the actual waveguide in terms of so called local normal modes. These modes are identical in form with the exact mode solutions of the uniform guide. However, the guide dimensions appearing as parameters in the mode expressions and the eigenvalue equation are now allowed to be functions of  $z$  to conform exactly to the actual shape of the nonuniform waveguide. These modes are not themselves solutions of Maxwell's equations because their parameters are function of  $z$ . However, they can be superimposed to yield the desired solution. This approach results in mode coupling coefficients that vanish everywhere except on the tapered portion and is used in simulating the extended interaction cavity. The other way is to use the normal modes in a uniform waveguide as the base for field expansion. This latter approach is more convenient for handling waveguide with periodic varying cross-section.

Substituting Eqs. (6) and (7) into Maxwell's equations in three dimensions, for each TE mode, their governing equations can be reduced to an equivalent set of one dimensional, time dependent, inhomogeneous transmission line equations<sup>4,6</sup>.

$$\frac{\partial E_{Tmn}}{\partial t} = -c \frac{\partial B_{Tmn}}{\partial z} + \omega_{cmn} B_{Lmn} - c B_{Tmn} \frac{r_w'(z)}{r_w(z)} \left( \frac{m^2}{k_{mn}^2 - m^2} \right) + c \frac{r_w'(z)}{r_w(z)} \sum_{l \neq n} K_{mnl} B_{Tml}$$

$$\begin{aligned}
& - \frac{2L_p}{N_p U_{mn}} \left( \frac{\omega_B}{\omega_{c0}} \right)^2 \frac{r_w(0)}{r_w(z)} \cdot \sum_j [V_{xj} e_{xmn}(x_j, y_j) + V_{yj} e_{ymn}(x_j, y_j)] \\
\frac{\partial B_{Tmn}}{\partial t} &= -c \frac{\partial E_{Tmn}}{\partial z} + c E_{Tmn} \frac{r_w'(z)}{r_w(z)} \left( \frac{m^2}{k_{mn}^2 - m^2} \right) + c \frac{r_w'(z)}{r_w(z)} \sum_{l \neq n} K_{mnl} E_{Tml} \frac{(1 - m^2/k_{ml}^2)}{(1 - m^2/k_{mn}^2)} \\
\frac{\partial B_{Lmn}}{\partial t} &= -\omega_{cmn} E_{Tmn} \quad . \quad (12)
\end{aligned}$$

Here  $\omega_{cmn} = ck_{mn}/r_w(z)$  is the waveguide cutoff frequency,

$$\begin{aligned}
\left( \frac{\omega_B}{\omega_{c0}} \right)^2 &= \frac{5.875 \times 10^{-5} I_b}{K_{\perp 0}^2 \beta_{z0}^2}, \quad K_{\perp 0}^2 = \frac{r_w(0) \omega_{c0}}{c}, \quad U_{mn} = J_m^2(k_{mn}) (1 - m^2/k_{mn}^2) \\
K_{mnl} &= \frac{2 k_{mn} k_{ml} J_m(k_{ml})}{(k_{ml}^2 - k_{mn}^2) J_m(k_{mn})}
\end{aligned}$$

and the electron beam is modeled by a collection of  $N_p$  macroelectrons distributed over length  $L_p$ . Each macroelectron represents  $N \cdot L_p / N_p$  electrons where  $N$  is the number of electrons per unit length. Here,  $c$  is the speed of light,  $\omega_{c0}$  is  $ck_{mn}/r_w(0)$ ,  $\vec{V}_j$  is the electron velocity, and  $\beta_{z0}$  is the average beam axial velocity divided by  $c$ . In order to avoid the singularity at cavity axis in advancing electron trajectories, the calculations are carried out using Cartesian coordinates. The  $x$  and  $y$  components of the transverse field functions  $\vec{e}_{\perp mn}^p$  and  $\vec{b}_{\perp mn}$  are given by

$$\begin{aligned}
e_{xmn}^{1,2} &= b_{ymn}^{1,2} = \mp \left[ J_{m-1} \left( \frac{k_{mn} r}{r_w(z)} \right) \begin{Bmatrix} \sin(m-1)\theta \\ \cos(m-1)\theta \end{Bmatrix} + J_{m+1} \left( \frac{k_{mn} r}{r_w(z)} \right) \begin{Bmatrix} \sin(m+1)\theta \\ \cos(m+1)\theta \end{Bmatrix} \right] \\
e_{ymn}^{1,2} &= -b_{xmn}^{1,2} = \mp \left[ J_{m-1} \left( \frac{k_{mn} r}{r_w(z)} \right) \begin{Bmatrix} \sin(m-1)\theta \\ \cos(m-1)\theta \end{Bmatrix} - J_{m+1} \left( \frac{k_{mn} r}{r_w(z)} \right) \begin{Bmatrix} \sin(m+1)\theta \\ \cos(m+1)\theta \end{Bmatrix} \right]
\end{aligned}$$

and

$$b_{zmn}^{1,2} = 2 J_m \left( \frac{k_{mn} r}{r_w(z)} \right) \begin{Bmatrix} \sin m\theta \\ \cos m\theta \end{Bmatrix} \quad . \quad (13)$$

The electromagnetic fields for the  $TE_{mn}$  mode acting on the electrons are then given by

$$\vec{E}_{mn} = \frac{r_w(0)}{r_w(z)} \sum_{p=1,2} E_{Tmn}^p \vec{e}_{\perp mn}^{(p)}$$

$$\vec{B}_{mn} = \frac{r_w(0)}{r_w(z)} \sum_{p=1,2} [ B_{Tmn}^p \vec{b}_{\perp mn}^{(p)} + \hat{z} B_{Lmn}^p b_{z mn}^{(p)} ]. \quad (14)$$

Following the approach of Solymar<sup>7</sup>, the waveguide radius in this scheme is allowed to be an arbitrary continuous function of axial position, allowing one to model profiled interaction circuits and mode conversion. The axial spatial dependence of the electromagnetic field is still represented by the Fourier series expansion and the leap-frog scheme for electron pushing in PIC codes is retained. The out-going wave boundary conditions are imposed along the axial direction. The code is stretched in the sense that the electromagnetic field allows only one dimensional (axial) spatial evolution but is used to simulate three spatial dimensional phenomena. This version of code is called stretched PIC code in plasma physics. These sets of equations appeared first in 1982 in Caplan's Ph.D dissertation<sup>3</sup>. He also used an effective damping rate for the electric component of the electromagnetic field to simulate the waveguide wall resistivity.

#### D. Space Charge Field

In a cylindrical waveguide, the transverse mode is a global mode and a finite number of modes is often sufficient to represent the electron-electromagnetic wave interaction. On the other hand, for electrostatic problems the fields outside the beam location decay exponentially, with no spatial oscillation and no wave propagation. To simulate this localized field, a great many transverse modes are needed along the radial direction. As a result, the scheme of using finite-differencing or B-spline are a better approach to evaluate the electrostatic field. The B-spline<sup>8-10</sup> of fourth order will be used to solve the two-dimensional Poisson equation in cylindrical coordinates

$$\frac{\partial^2 \Phi}{\partial r^2} + \frac{1}{r} \frac{\partial \Phi}{\partial r} + \frac{\partial^2 \Phi}{\partial z^2} = -4\pi\rho, \quad (15)$$

with the boundary conditions of  $\Phi(r,0) = \Phi(r,L) = \Phi(r_w,z) = 0$ . Expand the functions  $\Phi$  and  $\rho$  along the  $z$ -direction in terms of sine functions

$$\Phi = \sum_{k=1}^{N_z} \Phi_k(r) \sin \frac{k\pi}{L} z, \quad \rho = \sum_{k=1}^{N_z} \rho_k(r) \sin \frac{k\pi}{L} z, \quad (16)$$

where  $N_z$  is the number of grid points in the  $z$ -direction. Both sine and cosine functions should be used in the case of periodic axial boundary conditions. Substituting Eq.(16) into Eq.(15) yields

$$\Phi_k'' + \frac{1}{r} \Phi_k' - \left( \frac{k\pi}{L} \right)^2 \Phi_k = -4\pi\rho_k, \quad (17)$$

where prime denotes taking derivative with respect to the  $r$  coordinate.

The collocation method with B-splines is used to numerically solve Eq.(17). Let  $\{r_i\}_1^{N_r}$  be the radial grid points (knots),  $0 = r_1 < \dots < r_{N_r} = r_w$ . The solution of Eq.(17)



can be approximated by a spline  $S$  of fourth order on the grid  $\{r_j\}$ . A spline can be expressed in the following form

$$S(r) = \sum_{i=1}^n a_i B_i(r) \quad , \quad (18)$$

where  $B_i(r)$  are so called B-splines which are basic functions of the space of all cubic splines on the grid  $\{r_i\}$ .  $n = N_r + 2$  is the dimension of this space.

A Spline function is a function consisting of polynomial pieces on subintervals, joined together with certain smoothness conditions and is used in PIC code for interpolation.

$$B_i^0(r) = \begin{cases} 1 & \text{if } t_i \leq r < t_{i+1} \\ 0 & \text{otherwise} \end{cases}$$

This is the B-splines of degree 0. To generate all the higher B-splines, the simple recursive definition can be used

$$B_i^k(r) = \left( \frac{r-t_i}{t_{i+k}-t_i} \right) B_i^{k-1}(r) + \left( \frac{t_{i+k+1}-r}{t_{i+k+1}-t_{i+1}} \right) B_{i+1}^{k-1}(r) \quad (k \geq 1)$$

$$\sum_{i=1}^n B_i^k(r) = 1 \quad \text{for all } r$$

Substituting  $S(r)$  for  $\Phi(r)$  in Eq.(16) yields

$$\sum_{i=1}^n a_i^{(k)} \left[ B_i'' + \frac{1}{r} B_i' - \left( \frac{k\pi}{a} \right)^2 B_i \right] = -4\pi\rho_k \quad (19)$$

Since the values of  $\rho_k$  are known at the grid point  $r_j$ , we will evaluate Eq.(19) at these points to determine the coefficients  $a_i^{(k)}$ .

$$\sum_{i=1}^n a_i^{(k)} \left[ B_i''(r_j) + \frac{1}{r_j} B_i'(r_j) - \left( \frac{k\pi}{a} \right)^2 B_i(r_j) \right] = -4\pi\rho_k(r_j) \quad , \quad (20)$$

$j = 2, 3, \dots, N_r$

Because the term  $\frac{\Phi'}{r}$  in Eq.(11) is singular at  $r=0$ , we must treat it carefully. The property of axis-symmetry implies  $E_r = -\Phi' = 0$  at  $r=0$ . The L'Hospital rule is used to evaluate this singular term

$$\lim_{r \rightarrow 0} \frac{1}{r} \Phi' = \lim_{r \rightarrow 0} \Phi'' = \Phi''(0) . \quad (21)$$

Using Eq.(21), Eq.(20) at  $r=0$  becomes

$$\sum_{i=1}^n a_i^{(k)} [ 2B_i''(0) - \left( \frac{k\pi}{a} \right)^2 B_i(0) ] = -4\pi\rho_k(0). \quad (22)$$

Besides Eq.(20) and (22), we have two additional boundary conditions  $\Phi'(0) = 0$  and  $\Phi_k(r_w) = 0$ . In terms of B-splines, these become

$$\sum_{i=1}^n a_i^{(k)} B_i'(0) = 0 \quad \text{and} \quad \sum_{i=1}^n a_i^{(k)} B_i(r_w) = 0.$$

Now we have altogether  $N_r+2$  equations for  $N_r+2$  unknown coefficients  $a_i^{(k)}$  and the resulting equation can be written in the form of tridiagonal matrix. After  $a_i^{(k)}$  have been

evaluated, the electrostatic field can be determined from  $\vec{E}_s = -\nabla\Phi$ . In comparison with the conventional finite difference scheme, the present approach requires less storage spaces and is more accurate.

## E. Simulation Results

In order to validate the PIC code based on the mode expansion techniques, simulation results were compared with experiment, MAGIC, and theoretical prediction. In the following, only crucial results for the purpose of comparison are presented, the other detailed can be found in their respective references.

### a. Nonlinear Mode Interaction

In the experimental result on gyrotron traveling wave amplifier operated at the  $TE_{11}$  mode, it is observed that by increasing the injected power of the  $TE_{11}$  mode, the  $TE_{21}$  mode self-oscillation can be suppressed(Fig.1a). The following parameters were used in the experiment and the simulation:  $V_b=87.75\text{kV}$ ,  $I_b=1.25\text{A}$ ,  $\alpha=1$ ,  $r_w=0.2654\text{cm}$ ,  $B_0=12.38\text{kG}$ , and  $f_0=34.7\text{ GHz}$ . Since low current beam was used, only the TE modes were retained in simulations (space charge field is neglected) and the result was shown in Fig.1b. The agreement between them are very impressive. As a result, mutual verifications between the simulation and experiment were established and have strengthened the understanding of the multimode behavior and added to the predictability of high-power gyro-TWT's. Much physical insight into the multimode dynamics has been obtained with the valuable tool of numerical diagnostics which can be easily performed in simulations. The mechanisms for mode competition /suppression, for example, are clearly seen through the diagnostics of the perturbed beam distribution in momentum and energy spaces. Simulation results (Ref.[11]) clearly show that the

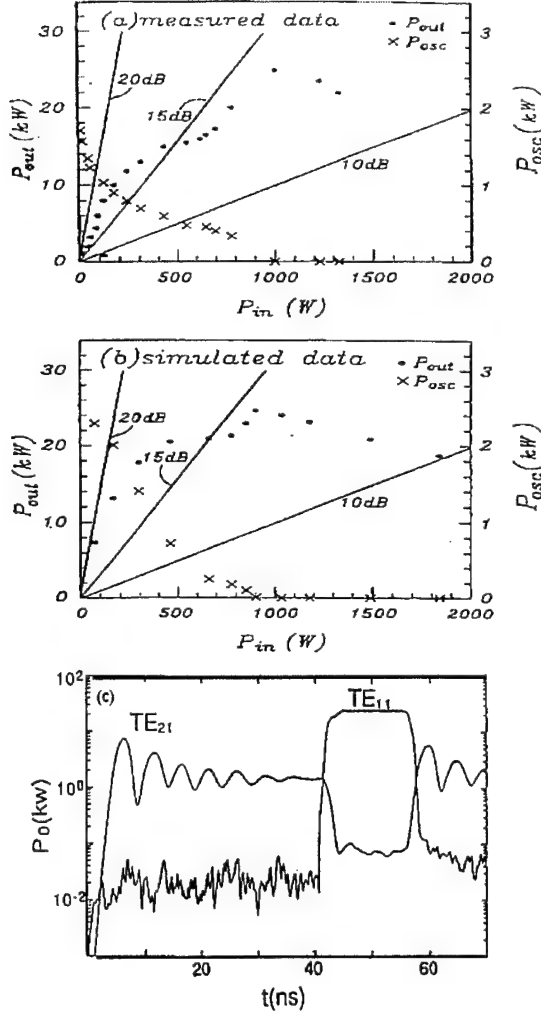


Fig. 1 Nonlinear mode interaction in Gyro amplifier (a) Measured TE<sub>11</sub> output power (filled circles) and TE<sub>21</sub> oscillation power (crosses) vs. the TE<sub>11</sub> drive. (b) Simulated data of the measurements in (a). (c) Time evolution of mode power. The beam is turned on at the reference time  $t = 0$ . The 900 W TE<sub>11</sub> drive is turned on at  $t = 42.5$  nsec and turned off at  $t = 58$  nsec.

performance of high power fundamental gyro backward wave oscillators with conducting axial boundary conditions, the following parameters were employed  $V_b = 350$  kV,  $I_b = 800$  A,  $\alpha = 1.5$ ,  $r_w = 4.37$  cm,  $B_0 = 3$  kG,  $L = 15$  cm, and guiding center  $r_g = 0.44 r_w$ .

In this high current device, the space charge field plays an important role in determining the efficiency. To verify that the present algorithm for evaluating space charge field is accurate, a simulation using the same parameters that were used in

organized beam perturbation associated with one mode appears as energy and velocity spread to another mode of different frequency or mode structure, and vice versa.

Mode competition processes are examined from a different perspective in Fig. 1c, which plots the temporal behavior of the spatially integrated wave power ( $P_0$ ) of the TE<sub>11</sub> and TE<sub>21</sub> modes. As soon as the electron beam is turned on at  $t = 0$ , the TE<sub>21</sub> mode grows spontaneously to a steady state following a few bounces caused by the instant turn-on of the beam. At  $t = 42.5$  nsec, a 900 W drive is injected, which grows to saturation in  $\sim 2$  nsec, a time scale comparable to the beam transit time through the waveguide. This is expected since the beam velocity and the TE<sub>11</sub> wave group velocity are approximately equal under the grazing resonance condition. Suppression of the TE<sub>21</sub> oscillation is mostly completed at  $t = 46$  nsec. But it is not until the TE<sub>11</sub> wave grows to a significant level that the oscillation level starts to diminish, a fact reflecting the nonlinear nature of mode-mode interactions. As the drive is turned off at  $t = 58$  nsec, TE<sub>21</sub> oscillation immediately comes back to the pre-drive level. This numerical sequence has precisely verified the experimental behavior.

#### b. Self-field Effects on High Power Gyro Backward Wave Oscillators

In a recent MAGIC simulation<sup>12</sup> carried out at Phillip's Laboratory, on the

MAGIC simulation was performed. The spatial axial momentum distribution at  $\omega_c t = 300$  from our simulations<sup>13</sup> that included both EM and ES fields (Fig.2a) is compared with the result from MAGIC code (Fig. 2b). The agreement between the two results using different algorithm is quite well.

### c. Plasma-filled Microwave Devices

To illustrate the effectiveness of separating the electric field into the electromagnetic and electrostatic components, a device operated at the TM mode must be simulated. In a recent long pulse ( $\tau = 120\mu s$ ) PASOTRON (Plasma Assisted Slow-Wave Oscillator) experiment<sup>14</sup>, the plasma was observed to totally neutralize the beam space charge field while no plasma return current was generated. The generation

of plasma return current can occur during the beam turn-on and turn-off periods. This is because a time varying beam current ( $J_b$ ) will induce a time varying  $B_\theta$  which in turn will produce an inductive  $E_z$  field to drive the plasma current. However, the effect arising from the edge of the beam pulse may not be important in a long pulse beam. The remaining  $J_b \hat{z} \times B_\theta \hat{\theta}$  force is capable of pinching the electron beam and thus substitute as the solenoidal magnetic field to confine the beam transport. In the experiment, the following parameters were used:  $V_b = 96kV$ ,  $I_b = 200A$ , average waveguide radius  $r_w = 3.25cm$ , wall ripple amplitude  $r_1 = .715cm$ , and ripple period  $z_0 = 2.4cm$ . The dispersion relation and growth rate for a periodic system using these parameters are given in Fig. 3a

in which the plasma density is assumed to be  $\omega_p = 0.6\omega_c$  ( $f_c = \frac{\omega_c}{2\pi}$ : waveguide cutoff frequency). Due to the difficulty in measuring the plasma density when the electron-wave interaction is taking place, the information on plasma density was not given in the experiment. The smooth wall Trivelpiece-Gould dispersion curve is a good approximation for plasma waves if the plasma column as a result of pinching is far away from the rippled wall boundary. This is due to the fact that plasma waves are localized inside the plasma column. The intersection "A" is the slow electromagnetic wave ( $TM_{01}$ ) and is absolutely unstable. If either beam current or interaction length exceeds the start oscillation threshold, the wave will grow from initial noise fluctuations and eventually saturate. On the other hand, the intersection "B" is convectively unstable. The wave will grow from the initial noise fluctuation at the entrance and convect out of the interaction region without strongly interfering with the evolution of mode "A". However, the growth

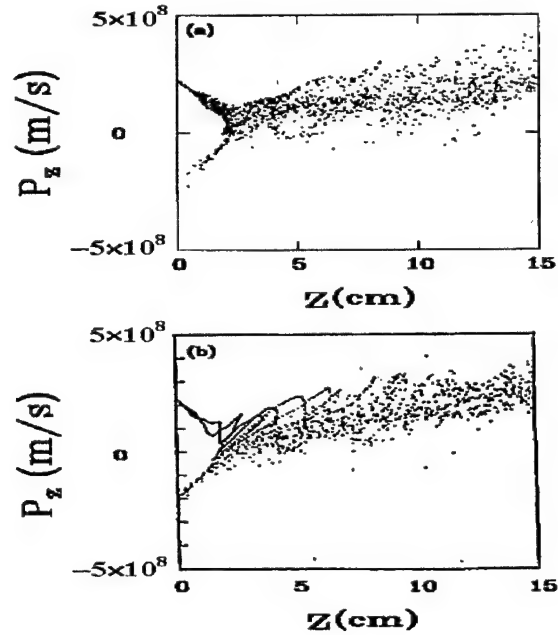


Fig. 2 Comparison of electron momentum axial spatical distribution from (a) our code and (b) MAGIC code.

rate of mode "A" is rather small even in an infinite system (Fig. 3a). In a real experiment, the finite length effect will further reduce the growth rate. It is quite possible that without the reflection from mismatch between device components or other effects caused by the presence of plasmas to enhance the growth rate, the oscillator might be stable. Computer simulations did demonstrate that the presence of plasma is capable of enhancing the oscillator gain in addition to neutralizing the beam space charge field. However, only the result relevant to the electric field decomposition is presented. The frequency spectrum of the electromagnetic wave determined separately from beam and plasma

transverse currents ( $\vec{J}_t$ ) is shown in Fig. 3b for  $\omega_p = 0.6 \omega_c$ . The spectrum contains only one peak at about  $1.3 \omega_c$  for both cases and is very close to the frequency of intersection "A". Simulation results show no trace of space charge field and clearly demonstrate that the field arising from the solenoidal current contains only the electromagnetic component. The electrostatic frequency spectrum (Fig. 3b) evaluated from beam electrons peaks at the same frequency as that of the EM wave. This is due to the synchronism between the beam slow space charge wave and the slow electromagnetic wave. There is a secondary peak at the frequency of beam fast space charge wave. In the absence of BWO instability, the electrostatic plasma response peaks at the frequency of the Trivelpiece-Gould mode. The peak shifts to the frequency of beam slow space charge wave when the BWO instability is excited. The result of frequency spectra clearly demonstrates that the scheme of separating EM and ES works nicely.

#### d. Mode Conversion

The inhomogeneity of the waveguide cross-section in the tapered section provides the coupling (mode conversion) among various waveguide modes. This mode coupling process could affect the performance of the extended interaction cavity by determining the mode purity in electron-wave interaction for each individual cavity. In order to be

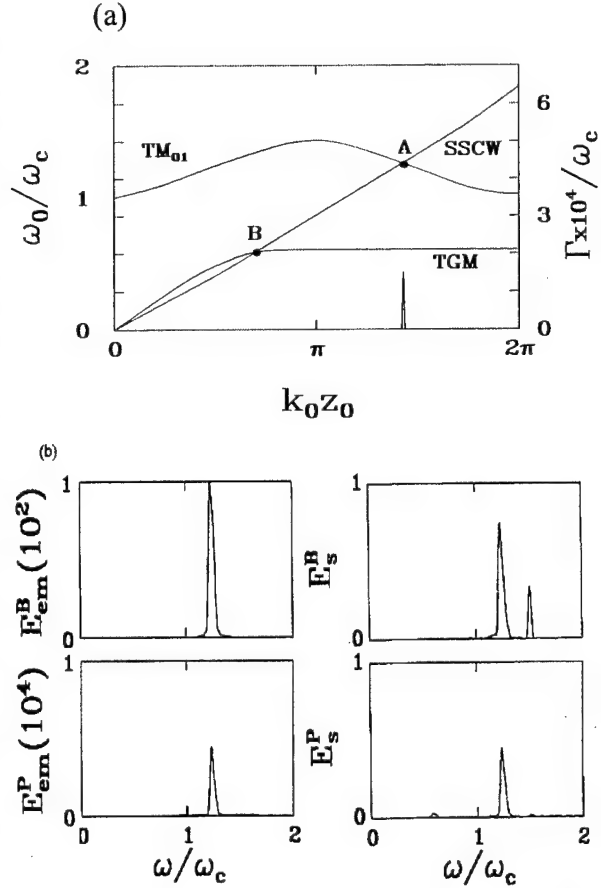


Fig. 3 Illustration of the electric field separation into EM and ES components using a plasma-filled device as an example (a) The dispersion relation of the  $TM_{01}$  mode, beam slow space charge wave, and plasma Trivelpiece-Gould mode. The growth rate for  $r_b = 0.25$  cm is also shown. (b) Frequency spectrum of EM and ES fields from beam and plasma.

sure that the stretched PIC code takes into account the mode conversion properly, simulation results<sup>15</sup> were compared with the theoretical prediction of Ref.[16]. According to Eq. (12), the coupling strength is proportional to the slope of the taper and inversely proportional to  $(k_{0l}^2 - k_{0n}^2)$ . In order to observe substantial mode conversion, a  $30^\circ$  taper angle and conversion between the  $TE_{02}$  and  $TE_{01}$  are chosen as an example for comparison. It is straightforward in simulation to include coupling to additional modes if necessary. The dimensions of gyrotron oscillator for simulation are shown in Fig. 4a. The mode profiles for the  $TE_{02}$  and  $TE_{01}$  modes from theoretical analyses (Ref. 16) are displayed in Fig. 4b. A 70 kV, 10 A beam with  $\alpha = 1.5$  and guiding centers located at 0.096 cm and  $B_0 = 35.54$  kG were used for simulations. The field profiles from our stretched PIC code simulation are shown in Fig. 4c which agrees quite well with Fig. 4b.

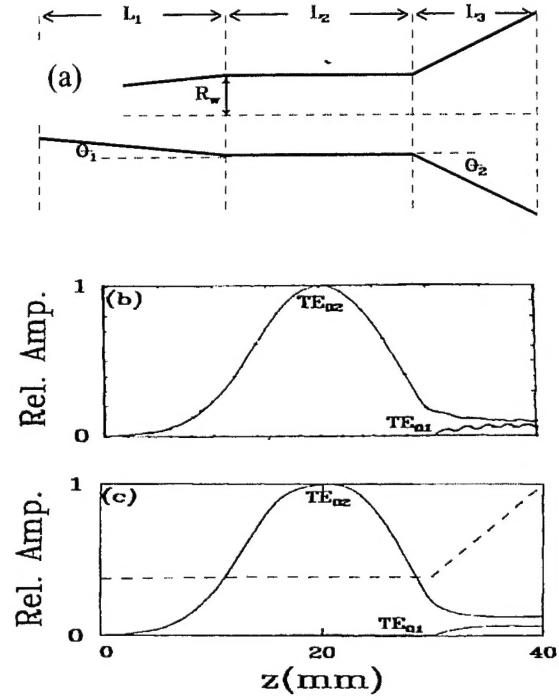


Fig. 4 Comparison of mode conversion in taper region. (a) Cavity dimensions,  $L_2 = 1.5$  cm,  $R_w = 0.37$  cm,  $\theta_1 = 0.5^\circ$ ,  $\theta_2 = 30^\circ$ . (b) Field profiles ( $TE_{01}$  and  $TE_{02}$ ) from theory. (c) Field profiles from simulation.

## II. Amplification Mechanism in The Output Section Of The Harmonic Multiplying Gyrotron Traveling Wave Amplifier

Particle-in-cell code simulations<sup>17</sup> have been carried out to investigate the physical mechanism responsible for the wave amplification in the output section of a harmonic-multiplying gyrotron traveling-wave tube. Simulation results demonstrate that the injected signal frequency plays an important role in determining the wave growth process. This is because the initial frequency mismatch as well as the resulting electron energy change in the input section influences the extent of bunching at the entrance of the output section and the slope of the electron phase trajectory. For a small frequency mismatch, the amplification arises entirely from the second harmonic generation due to the bunching at the fundamental frequency. As the mismatch is increased, the bunched electrons start to disperse early in the output section; and the wave amplification is then dominated by the cyclotron maser instability. The electron velocity spread is observed to substantially degrade the device performance.

By using the combination of a waveguide input section ( $L_i$ ,  $TE_{02}$ ) that amplifies the input signal at the fundamental cyclotron frequency, a drift section ( $L_d$ ), and an output waveguide section ( $L_o$ ,  $TE_{03}$ ) that generates the output wave at the second harmonic

cyclotron frequency, the bandwidth of the phigtron<sup>18</sup> can be substantially improved. The above harmonic-multiplying scheme made the source for the input signal more readily available, reduces the magnetic weight requirement, and alleviates the stability problem.

The frequency-multiplying amplification process in the TWA output section is rather involved and remains to be addressed. There are at least two physical mechanisms that could give rise to the wave amplification process. The conventional thinking is that the amplification process is entirely due to the second harmonic cyclotron maser instability and the instability is believed to be initiated by the beam second harmonic current component in the bunched electrons. On the other hand, in the harmonic-multiplying gyrotron TWT, the electron beam is pre-bunched at the fundamental frequency before entering the output waveguide. This fundamental bunching will continue into the output section until the electrons start to cross one another or the self-consistent field grows to large amplitude to alter the electron motion. In a conventional klystron, the bunched electrons induce the electromagnetic field in the output cavity with the proper phase to slow the beam down and convert the beam kinetic energy into coherent radiation without invoking any instability. Similarly, the second harmonic RF current associated with the fundamental bunching can induce an electromagnetic wave with the proper phase supported by the output waveguide to slow down the beam. The latter mechanism can be isolated in simulations by setting the self-consistent field to zero and thus breaking the closed feedback loop for the instability.

The parameters used in simulations for a 35 GHz harmonic-multiplying gyro-TWT are  $V_b = 50\text{kV}$ ,  $I_b = 30\text{A}$ ,  $\alpha = 1.5$ ,  $L_i = 10\text{cm}$ ,  $L_d = 14\text{cm}$ ,  $L_o = 20\text{cm}$ , and  $B_0 = 6.068\text{kG}$ . In order to determine the effect of varying the frequency mismatch ( $\Delta\omega$ ) between the Doppler-shifted wave frequency and the electron cyclotron frequency on the gain mechanism in the output waveguide, three cases with different input frequency are simulated. The spatial evolution of the second harmonic wave and the electron phase trajectories of 30 test electrons in the output waveguide are displayed in Fig. 5. The electron phase trajectory with respects to the fundamental cyclotron frequency is evaluated without the effect of the RF field in the output waveguide according to  $\phi_i(z) = \phi_i(0) + [\frac{\Omega_c}{\gamma_i(z)} - \frac{\Omega_c}{\gamma_i(0)}]T$ , where the argument 0 is at the electron injected plane and T is the time elapsed. Using  $\omega_i = 1.03\omega_c$  ( $f_c$  is the cutoff frequency of the input waveguide), the initial frequency mismatch  $\Delta\omega$  is  $0.01\omega_c$ . With this input frequency, the wave amplification (Fig. 5a) that takes the self-consistent field into account follows very closely the result from the fundamental bunching alone (turn off the effect the self-consistent field on electron motion). The electrons remain bunched throughout the output waveguide and the optimized efficiency is about 16%. Increasing  $\omega_i$  to  $1.06\omega_c$  ( $\Delta\omega = 0.015\omega_c$ ), the optimized efficiency is increased to 22% (Fig. 5b). The result shows that the bunch starts to disperse at about  $z_s = 10\text{ cm}$  and at about the same time the induced field from the fundamental bunching saturates. After  $z_s$  the cyclotron maser instability dominates the gain process. Increasing  $\omega_i$  further to  $1.08\omega_c$  ( $\Delta\omega = 0.0195\omega_c$ ). The optimized efficiency reduces to only 8.6% (Fig.1c). In this case, the gain process is dominated by the cyclotron maser instability with reduced growth rate due to the large beam energy spread caused by the dispersion of fundamental bunching. The



understanding of the gain mechanism in the output waveguide will have important implication for the design of future experiments.

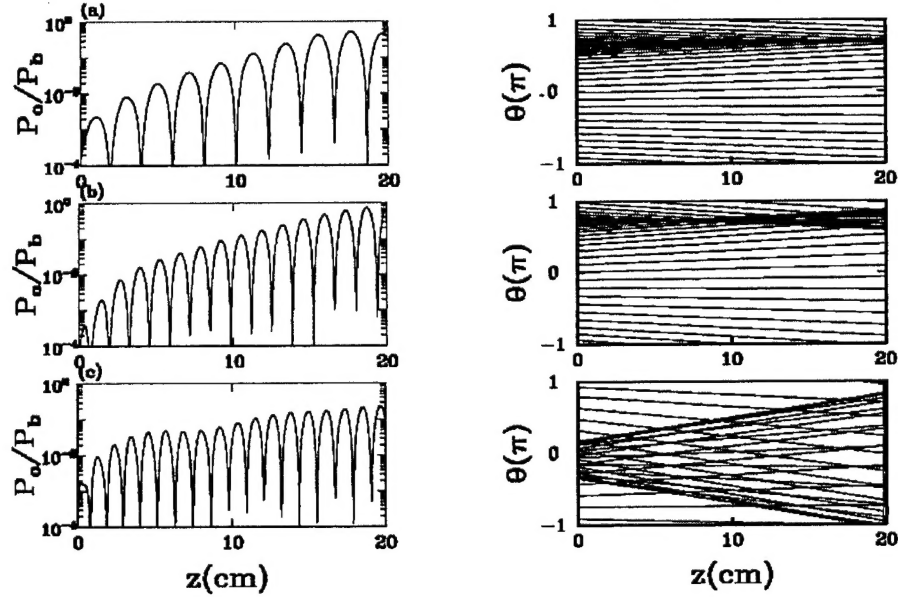


Figure 5. Spatial evolution of the second harmonic wave and electron phase trajectories of 30 test electrons in the output waveguide.  
(a)  $\omega_i = 1.03$  (b)  $\omega_i = 1.06$  (c)  $\omega_i = 1.08$ .

### References:

1. B. Goplen, L. Ludeking, D. Smithe, and G. Warren, "User-Configurable MAGIC for Electromagnetic PIC Calculations," *Computer Physics Communication*, **87**, 54(1995).
2. A. T. Lin, J. M. Dawson, and H. Okuda, "Application of Electromagnetic Particle Simulation to the Generation of Electromagnetic Radiation," *Phys. Fluids*, **17**, 1995(1974).
3. J. M. Dawson and A. T. Lin, "Particle Simulations," *Handbook on Plasma Physics*, Vol. II, Basic Plasma Physics. A. A. Galeev and R. N. Sudan, Eds., (Elsevier Science Pub., Amsterdam) Chapter 7, p. 555 (1984).
4. M. Caplan, "Application of the relativistic bunching of electrons to the generation of intense millimeter microwave radiation," Ph. D. Dissertation. UCLA(1986).
5. J. D. Jackson, "Classical Electrodynamics," Chapter 6, (Wiley, 1975).
6. M. Caplan, A. T. Lin, and K. R. Chu, "A study of the Saturated Output of a TE<sub>01</sub> Gyrotron Using an Electromagnetic Finite Size Particle Code," *Int. J. Elec.*, **53**, 659(1982).
7. L. Solymar, "Spurious mode generation in non-uniform waveguide," *IRE Trans. on Microwave Theory and Techniques*, Vol. MTT-7, p. 379(1959).



8. C. DeBoor, "Package for Calculating with B-Splines," SIAM J. Numer. Anal., 14, 441(1977).
9. C. DeBoor and B. Swartz, "Collocation at Gaussian Points," SIAM J. Numer. Anal., 10, 582(1973).
10. D. Trunec, J. Drimal, and M. Vicar, "A Subprogram for Direct Solution of Poisson Equation in Cylindrically Symmetric Geometry," Computer Physics Communications, 98, 339(1996).
11. K. R. Chu, L. R. Barnett, W. K. Lau, L. H. Chang, A. T. Lin and C. C. Lin, "Nonlinear Dynamics of the Gyrotron Traveling Wave Amplifier," Phys. Fluids, B3, 2403(1991).
12. T. A. Spencer and M. D. Stump, "Dynamics of the Space Charge Limiting Current in Gyro-Type Devices," Conference Record, 1997 IEEE Int. Conf. on Plasma Science, p. 257(1997).
13. Chih-Chien Lin and A. T. Lin, "A new algorithm for solving Maxwell's equation in high-power microwave device simulations," IEEE Trans. on Plasma Science, Vol. 26, p. 893(1998).
14. D. M. Goebel, et. al., "High-Power Microwave Source Based on an Unmagnetized Backward-Wave Oscillator," IEEE Trans. on Plasma Science, 22, 547(1994).
15. E. Borie and B. Jödicke, "Resonator design studies for a 150 GHz Gyrotron at KfK," Int. J. Electronics, Vol. 64, p. 107(1988).
16. A. T. Lin, H. Guo, and V. L. Granatstein, "Dynamic Simulation of Mode-Selective Interaction Cavity for wide-Band High-Power Gyrotron Applications," IEEE Trans. On Plasma Science, 28, 782(2000).
17. A. T. Lin and Chih-Chien Lin, "Amplification Mechanism in The Output Section of The Harmonic Gyrotron Traveling Wave Amplifier," IEEE Trans. On Plasma Science, Vol. 28, June (2002).
18. H. Guo, S. H. Chen, V. L. Granatstein, J. Rodgers, G. S. Nusinovich, M. T. Walter, J. Zhao, and W. Chen, "Operation of a high performance, harmonic-multiplying, inverted gyrotwyston," IEEE Trans. on Plasma Science, Vol. 26, P. 451, 1998.